Journal of Materials Chemistry A



PAPER



Cite this: *J. Mater. Chem. A*, 2020, **8**, 16006

Molecular-level environments of intercalated chloroaluminate anions in rechargeable aluminum-graphite batteries revealed by solid-state NMR spectroscopy†

Jeffrey H. Xu, 📵 Ankur L. Jadhav, 📵 Damon E. Turney 📵 and Robert J. Messinger 🔘 *

Rechargeable aluminum-graphite batteries are an emerging energy storage technology with great promise: they exhibit high rate performance, cyclability, and a discharge potential of approximately 2 V, while both electrodes are globally abundant, low cost, and inherently safe. The batteries use chloroaluminate-containing electrolytes and store charge in the graphite electrodes when molecular AlCl₄ anions electrochemically intercalate within them. However, much remains to be understood regarding the ion intercalation mechanism, in part due to challenges associated with characterizing the chloroaluminate anions themselves. Here, we use solid-state ²⁷Al nuclear magnetic resonance (NMR) spectroscopy to probe the molecular-level electronic and magnetic environments of intercalated chloroaluminate anions at different states-of-charge. The results reveal broad ²⁷Al NMR signals associated with intercalated $AlCl_4^-$ anions, reflecting high extents of local disorder. The intercalated anions experience a diversity of local environments, many of which are far from the ideal crystalline-like structures often depicted in graphite staging models. Density functional theory (DFT) calculations of the total ²⁷Al isotropic shifts enable the contributions of chemical shift, ring-current effects, and electric quadrupolar interactions to be disentangled quantitatively. In combination, the solid-state NMR and DFT results reveal the molecular geometries and environments of intercalated AICl₄⁻ anions and capture the significant disorder present in intercalated graphite battery electrodes.

Received 6th March 2020 Accepted 29th June 2020

DOI: 10.1039/d0ta02611e

rsc.li/materials-a

Introduction

Rechargeable aluminum-graphite batteries using chloroaluminate-containing ionic liquid electrolytes have recently been demonstrated, wherein AlCl₄ chloroaluminate anions electrochemically intercalate into graphitic electrodes. 1-3 Depending on the graphite type, aluminum-graphite cells exhibit discharge plateaus of approximately 2 V and discharge capacities of up to 120 mA h g^{-1} . Numerous reports have also demonstrated their ultrafast discharge/charge capabilities, 2,4,5,7 long cycle lifetimes and high coulombic efficiencies at sufficiently fast rates, 5,6,9 and a wide operational temperature range (e.g., -40 °C to 120 °C).5,6 However, further technological improvements have plateaued, in part due to limited molecularlevel understanding of the ion intercalation mechanism, as the intercalation of molecular anions into graphite differs greatly from those involving atomic cations (e.g., Li⁺, Na⁺, etc.). Notably, there remain discrepancies among various experimental^{2,6,10} and

Department of Chemical Engineering, The City College of New York, CUNY, 160 Convent Avenue, New York, New York 10031, USA. E-mail: rmessinger@ccny.cuny.edu † Electronic supplementary information (ESI) available: Solid-state NMR sample preparation, additional NICS effects, ²⁷Al single-pulse MAS NMR spectrum of metallic aluminum and calculated EFG tensors. See DOI: 10.1039/d0ta02611e

computational¹¹⁻¹⁸ studies regarding the interlayer spacings and stage numbers of the intercalated graphite electrodes, as well the molecular geometries and environments of the intercalant anions. Over the past few years, aluminum–graphite batteries have been studied using a variety of techniques to reveal surface properties (*e.g.* XPS, AFM, SEM/EDS, TEM, *etc.*) or bulk properties (*e.g.* XRD, Raman, *etc.*) of the graphite electrodes. However, there have been no reports thus far that utilize techniques capable of revealing bulk properties of the intercalant anions themselves within the graphite electrode. In particular, solid-state ²⁷Al nuclear magnetic resonance (NMR) spectroscopy can directly probe the local electronic and magnetic environments of the intercalated chloroaluminate anions themselves and may shed light on the ion intercalation mechanism.

Previous studies have established solid-state NMR as a powerful tool to study ion-intercalated battery as well as supercapacitor electrodes, revealing molecular-level insights into their electrochemical charge storage mechanisms.¹⁹⁻²⁴ Solid-state NMR measurements are sensitive to the local environments and dynamics of intercalant ions, as well as ionion or ion-framework interactions of intercalant-electrode systems.²⁵ For example, for lithium-ion insertion into graphite or hard carbon electrodes, solid-state *ex situ*^{26,27} and

in situ^{28,29} ⁷Li NMR techniques have identified lithium in distinct environments (intercalated, pseudo-metallic, covalently bonded). Furthermore, solid-state ⁶Li and ⁷Li MAS NMR studies have also revealed local structure and disorder in lithium-intercalated positive electrode materials, such as transition metal oxides and polyanionic compounds. 30,31 Similarly, solid-state 23 Na NMR techniques (both $ex\ situ^{32}$ and in situ^{33,34}) have been employed on sodium-ion batteries, specifically to elucidate the Na⁺ insertion and deposition mechanisms at hard carbon cathodes and sodium metal anodes, respectively. While solid-state NMR has been previously used to study the intercalation of molecular anions such as hexafluorophosphate (PF₆⁻)³⁵ and bistriflimide (TFSI⁻)³⁶ into graphite, to our knowledge, it has not yet been used to study the local environments of intercalated AlCl₄ chloroaluminate anions.

Density functional theory (DFT) quantum chemical calculations aid interpretation of observable solid-state NMR signals, which are the result of different physical interactions. These methods have been used to calculate chemical shifts, nuclearindependent chemical shifts (NICS), and electric field gradient (EFG) tensors³⁷ for systems where species interact with various carbon structures such as porous carbons, 38,39 polycyclic aromatic hydrocarbons, 40 single-layer graphene 42 graphite.43 For example, Forse et al.39 studied the effects of different structural factors on DFT-derived NMR shifts, which were used to interpret experimental ¹⁹F NMR spectra of BF₄ anions adsorbed on titanium carbide-derived carbons. DFT has also been used to compute the molecular structures and energetics of other intercalating molecular species into graphite, such as PF₆⁻ anions, 44-46 ClO₄⁻ anions, 46 and TFSI⁻ anions, 47 with applications for positive electrodes for lithium and sodium batteries. 44-46 While DFT methods have been used to calculate energy-optimized structures of AlCl₄⁻ anions intercalated into graphite, they have not yet been used to predict ²⁷Al NMR parameters and shift values.

Here, we report solid-state ²⁷Al magic-angle-spinning (MAS) NMR measurements of natural graphite electrodes cycled to different states-of-charge to probe the molecular-level environments of intercalated AlCl₄ chloroaluminate anions at different extents of intercalation. The solid-state 27Al NMR spectra revealed broad ²⁷Al signals with varying shifts, linewidths, and longitudinal T_1 relaxation times associated with chloroaluminates in diverse local environments. To interpret the experimental ²⁷Al shifts, we performed DFT calculations on [AlCl₄]-coronene-based bilayer model systems with varying interlayer spacings to simulate structures with different AlCl₄⁻ molecular geometries and environments. The DFT calculations were used to compute contributions of the chemical shift, aromatic ring-current effects (nucleus-independent chemical shift), and electric quadrupolar interactions (quadrupolar shift) on the total ²⁷Al isotropic shift. The calculated total ²⁷Al isotropic shifts were correlated with the experimental ²⁷Al shifts to better understand the diversity of molecular configurations and intercalant-graphite interactions. The results, when analyzed as a function of state-of-charge, yield new molecularlevel understanding of the reversible electrochemical intercalation of AlCl₄ anions into graphite battery electrodes.

Methods

Cell assembly and electrochemical measurements

The experimental methods for electrode fabrication, cell assembly, and electrochemical testing are detailed in our previous work.4 Briefly, composite electrodes were prepared using natural graphite flakes (Alfa Aesar, 99.9995%) and poly(vinylidene fluoride) (PVDF) binder (Sigma-Aldrich, average molecular weight 534 000 g mol^{-1}) in a mass ratio of 90 : 10 on molybdenum (Mo) foil current collectors (Alfa Aesar, 99.95%, 0.025 mm thick). Cells were prepared using an aluminum foil negative electrode (MTI, 99.99%, 0.1 mm thick), a glass fiber separator (Whatman brand, GF/D), a natural graphite positive electrode, and an AlCl₃: [EMIm]Cl electrolyte (1.5:1 molar ratio, Iolitec, 30 µL) using polytetrafluoroethylene (PTFE) unions (Swagelok, 1/2-in. (12.7 mm) diameter, no. T-810-6) as airtight cell bodies and Mo current collector rods (Torrey Hills Technologies). Typical open circuit potentials for the aluminum-graphite cells were ca. 1.65 V. Galvanostatic cycling was performed on an Arbin LBT battery tester at 60 mA g⁻¹ using upper and lower voltage cut-off limits of 2.45 V and 0.50 V, respectively.

NMR sample preparation

After the aluminum-graphite cell's desired state-of-charge was reached, it was disassembled in an argon-filled glovebox (<1 ppm O₂ and H₂O levels). Excess electrolyte was removed from the graphite electrodes by rinsing with anhydrous methanol, soaking for 5 min, and then rinsing again. Anhydrous methanol was observed to be more effective at removing excess electrolyte than CCl₄, as measured by energy-dispersive X-ray Spectroscopy (EDS) (Fig. S1†). The electrode was dried in the glovebox for 20 min to allow the methanol to evaporate. The electrode material was then separated from the current collector, ground by mortar and pestle, and diluted with potassium bromide (Anhydrous, Sigma-Aldrich, ≥99%) using a mass ratio of 30:70 sample:KBr to improve MAS spinning stability by reducing the electrical conductivity of the composite sample. This sample:KBr mixture was then packed into 1.6 mm diameter zirconia rotors inside the argon-filled glovebox.

NMR spectroscopy

Solid-state 27 Al NMR measurements were acquired on a Bruker AVANCE III HD 600 MHz spectrometer with a 14.1 T narrow-bore superconducting magnet operating at 156.375 MHz for 27 Al nuclei, respectively. A PhoenixNMR 1.6 mm HXY MAS probehead was used. Samples were rotated at MAS rates of 10 kHz, which was limited due to the high conductivity of the graphite samples. Air at a temperature of 293.2 K was pumped through the probehead at $600\,\mathrm{l}\,\mathrm{h}^{-1}$ to mitigate sample heating due to MAS. Samples were spun at 10 kHz MAS for 6 hours before data collection to centrifugally separate any excess free electrolyte trapped in the pores of sample (Fig. S2†). Solid-state 27 Al single-pulse NMR

measurements were conducted using $\pi/2$ radio frequency (rf) pulses of 1.9 μ s (131.6 kHz rf field strength). Note that both $\pi/12$ and $\pi/2$ rf pulses yielded identical solid-state ²⁷Al NMR spectra, indicating that single-pulse experiments with $\pi/2$ rf pulses were quantitative. 48 Longitudinal (T_1) and transverse (T_2) relaxation time measurements were performed using the inversion-recovery and variable-delay spin-echo pulse sequences, respectively. Recycle delays of 0.25 s were used for all experiments, which were calibrated to ensure that all ²⁷Al nuclear spins relaxed to equilibrium ($>5T_1$) and that all spectra are fully quantitative. Absolute spectral intensity was normalized by sample mass. ²⁷Al shifts were referenced to a 1 M aqueous solution Al(NO₃)₃ at 0 ppm. Spectral deconvolutions were performed with the DMFit software.49 All 27Al signals associated with intercalated chloroaluminate species were modeled as a mixed Gaussian/ Lorentzian lineshape (e.g., 0.5:0.5 Gaussian:Lorentzian ratio for the dominant ²⁷Al NMR signal), while those associated with the liquid electrolyte were modeled as pure Lorentzian lineshapes.

DFT calculations

Gaussian09 (ref. 50) was used to perform all ²⁷Al magnetic shielding tensors and electric field gradient tensor calculations. Ground-state DFT methods using a 6-31G(d) basis set and the hybrid B3LYP functional (Becke's three-parameter nonlocal exchange functional and Lee-Yang-Parr's correlation functional) were used for all geometry optimization and gauge-independent atomic orbital (GIAO) NMR calculations of coronene-based structures, following Moran et al. 40 and Forse et al. 39 to optimize similar structures. The coronene-based bilayers were constructed using an AB stacking (Bernal) structure and the van der Waals dispersion correction (D3) developed by Grimme et al.51 The structures of the coronene-based bilayer and AlCl₄⁻ molecule were first optimized independently. To construct the graphite intercalation compound, the optimized AlCl₄ structure was inserted into the central point of the optimized bilayer coronenebased structure (vertically (c-axis) and laterally (a- and b-axes)). Atom Groups were used to assign charges to the coronene-based bilayer (+1) and the $AlCl_4$ (-1). For calculations involving incremental changes of the bilayer d-spacing and ion lateraldisplacement, the geometry of the AlCl₄⁻ molecule was first reoptimized using fixed carbon and aluminum atomic coordinates and a Universal Force Field (UFF) in Avogadro Molecular Editor.⁵² A chemical shielding value for [Al(H₂O)₆]³⁺ of 611 ppm [B3LYP/6-31G(d)] was used as the reference to convert ²⁷Al magnetic shielding values to ²⁷Al chemical shift values. The ions in the electrolyte (non-intercalated) were modeled as an [AlCl₄⁻] [EMIm⁺] ion pair using the B3LYP-D3 basis set, as recommended for DFT calculations of imidazolium-based ionic liquids.53

Results and discussion

Liquid-state ²⁷Al NMR measurements were first performed on the AlCl₃:[EMIm]Cl ionic liquid electrolyte to characterize the choloraluminate anions before intercalation into graphite. The liquid-state single-pulse ²⁷Al NMR spectrum (Fig. 1) reveals overlapping ²⁷Al signals that can be deconvoluted into two

purely Lorentzian components at 103.2 and 97.4 ppm associated with AlCl₄ and Al₂Cl₇, respectively. The relative populations of AlCl₄⁻ and Al₂Cl₇⁻ species, obtained by their relative integrated ²⁷Al signal intensities, were measured to be 90% and 10%, consistent with Ferrara et al. ⁵⁴ The ²⁷Al longitudinal (T_1) relaxation times were 200 and 290 µs for AlCl₄ and Al₂Cl₇, respectively. The longer 27 Al T_1 relaxation time for the dimeric species is due to slower stochastic fluctuations of the EFG as a result of its larger size and slower molecular motions (e.g., rotations). Both ²⁷Al signals associated with the chloroaluminate anions exhibited single-exponential T_1 relaxation, as opposed to multi-exponential, consistent with fast isotropic motions in the liquid-state and relaxation behavior within the extreme narrowing limit.54 Accordingly, the 27Al transverse relaxation time (T_2) times were identical to the T_1 relaxation times.

Molecular-level environments of intercalated chloroaluminate anions elucidated by solid-state ²⁷Al NMR

To probe the molecular-level environments of AlCl₄⁻ anions intercalated within the graphitic layers, solid-state single-pulse ²⁷Al MAS NMR measurements were performed on electrodes cycled to various states-of-charge (Fig. 2) that correspond to inflection points on the voltage *vs.* time galvanostatic cycling profiles, at which key electrochemical events associated with the formation of periodically-ordered graphite intercalation compounds occur.⁴ The solid-state ²⁷Al NMR spectrum of an electrode that was harvested at the open-circuit potential (noncycled) of 1.65 V, left for 24 hours after cell assembly (point A) and rinsed with anhydrous methanol, shows no ²⁷Al signal intensity. This result establishes that methanol successfully removed the excess electrolyte and that no solid reaction products were formed.

The solid-state ²⁷Al NMR spectra reveal ²⁷Al signals that increase in intensity upon charge and decrease in intensity upon discharge, reflective of the changing populations of chloroaluminate species intercalated within the graphite electrode (Fig. 2). The NMR spectra and their deconvolutions reveal three ²⁷Al components: (i) an intense and broad ²⁷Al signal,

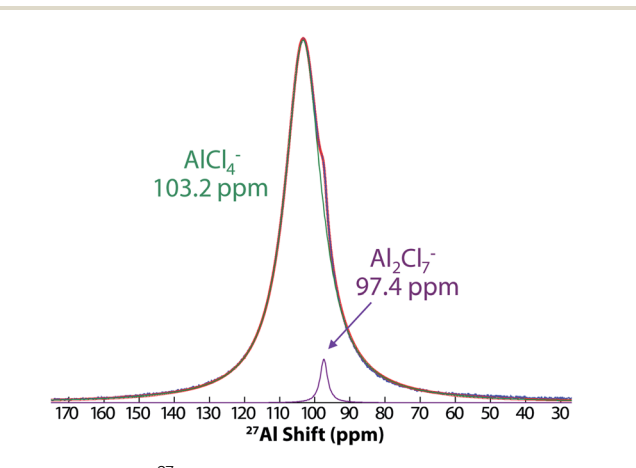


Fig. 1 Liquid-state 27 Al single-pulse NMR spectrum of bulk AlCl $_3$: [EMIm] Cl (molar ratio 1.5 : 1) ionic liquid electrolyte.

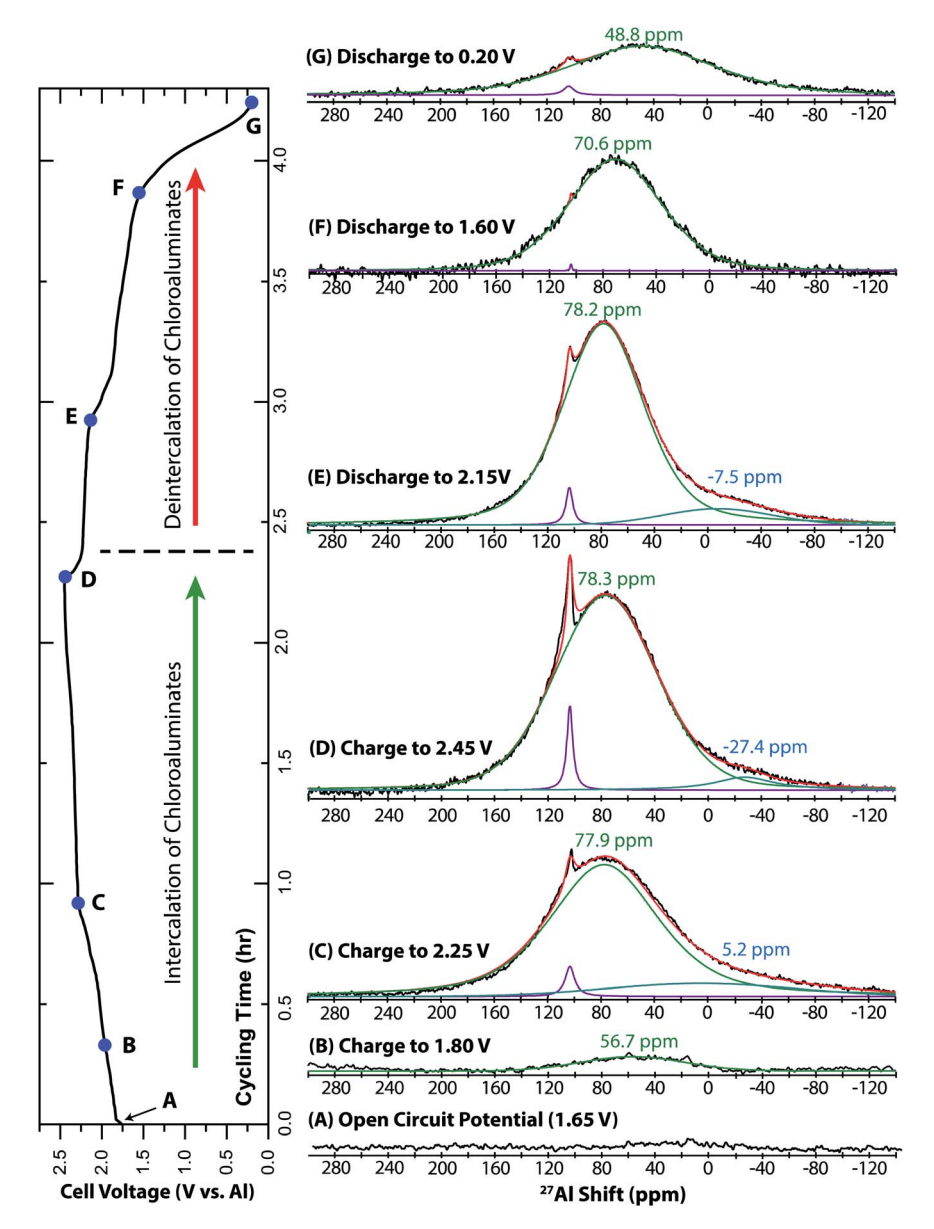


Fig. 2 Solid-state 27 Al single-pulse MAS NMR spectra (right) of natural graphite electrodes from aluminum—graphite cells galvanostatically cycled to specified states-of-charge at 60 mA g^{-1} (left), acquired under conditions of 10 kHz MAS at 14.1 T. Point (A) represents an electrode from a cell, never cycled, that remained at the open-circuit potential for 24 h. Quantitative deconvolutions of the NMR spectra are shown. The dominant 27 Al signal (e.g., 78.3 ppm, Point D) is associated with AlCl₄ $^-$ chloroaluminate anions intercalated into graphite.

ranging from 48.8 to 78.3 ppm, associated with $AlCl_4$ chloroaluminate anions that are intercalated within the graphite layers, (ii) a sharp signal at ca. 103 ppm attributed to residual bulk electrolyte, and (iii) a lower-intensity broad signal centered below 10 ppm whose origin is unclear, but whose shift is consistent with octahedrally-coordinated aluminum species. Note that adsorbed chloroaluminate anions compose a negligible fraction of the ^{27}Al NMR signals due to the low specific surface area of natural graphite (4.4 m 2 g $^{-1}$, as measured by N $_2$ sorption) relative to the total interlayer surface area available for intercalation. As shown in our prior work, 4 capacity attributed to surface effects, such as double-layer capacitive charging or faradaic electrochemical reactions of adsorbed ions, are expected to account for <1% of the total capacity. Instead, the

observed capacity is due to the electrochemical intercalation of ${\rm AlCl_4}^-$ anions into the graphite layers.

Analyses of the main broad ²⁷Al signal associated with intercalated AlCl₄⁻ species reveal insights into their local environments at different states-of-charge. ²⁷Al NMR shifts and linewidths (full-width-half-maximum, FWHM, of Gaussian lineshape) are shown in Fig. 3a and b, respectively. Upon charging from the open-circuit potential of 1.65 V (point A) to 1.90 V (point B), chloroaluminate anions begin to electrochemically intercalate within the graphite layers without establishing ordered graphite staging (*i.e.*, only dilute staging present⁵⁵) as evidenced by *in operando* XRD measurements below 2.06 V.¹⁰ The corresponding ²⁷Al NMR spectrum reveals a broad ²⁷Al signal centered at 56.7 ppm (FWHM of 108 ppm),

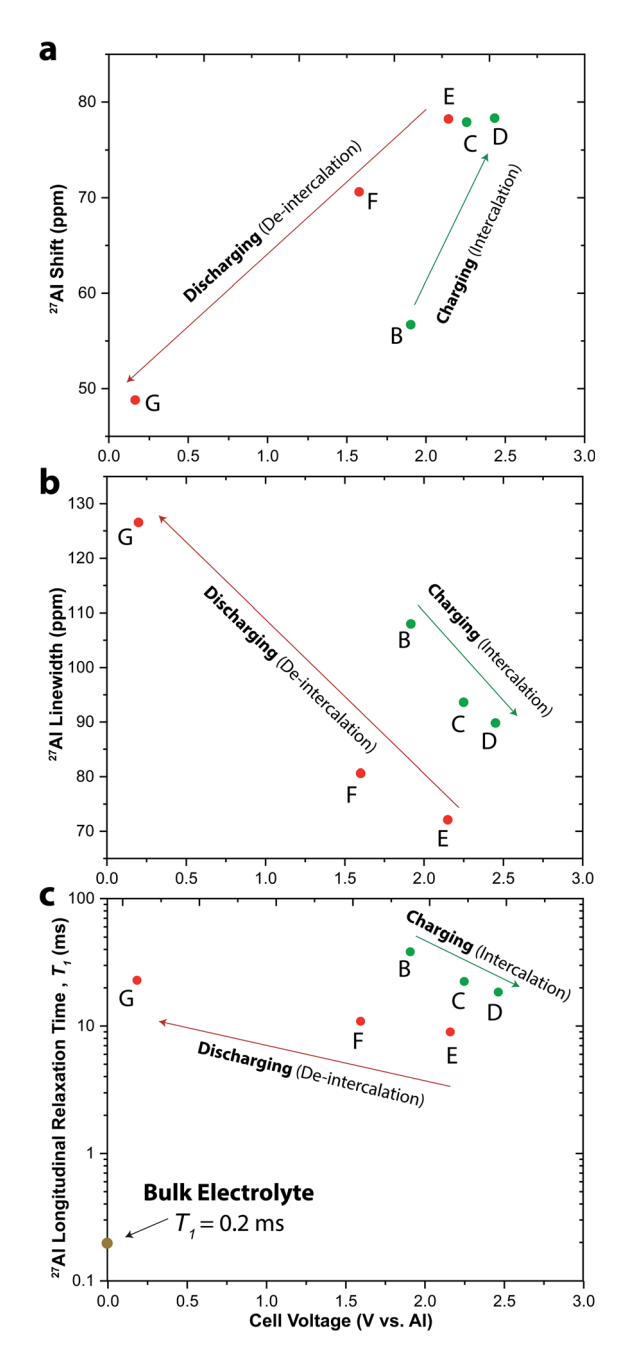


Fig. 3 Analyses of the solid-state 27 Al NMR signals attributed to AlCl $_4$ anions intercalated within natural graphite. (a) Average 27 Al shifts, (b) 27 Al signal linewidths (full-width-at-half-maximum), and (c) 27 Al longitudinal T_1 relaxation times.

which is associated with $AlCl_4$ chloroaluminate anions in distorted geometries, as discussed below. After charging to 2.25 V (point C) and 2.45 V (point D), chloroaluminate species continue to intercalate, resulting in graphite interlayer expansion and staging. The ²⁷Al signals associated with intercalated $AlCl_4$ species shifts to *ca.* 78 ppm and its linewidths decreases, likely because the intercalated molecular anions reside in less distorted and modestly more uniform environments. The average ²⁷Al NMR shift of an intercalated chloroaluminate species is 78.3 ppm (point D). Nevertheless, the broad

distributions of ²⁷Al chloroaluminate environments, reflected in the broad lineshapes (FWHM of 90 ppm, point D), are a direct manifestation of the underlying heterogeneity and disorder of the graphite structure. The intercalated chloroaluminate anions thus experience a diversity of magnetic and electronic environments, many of which are far from the idealized, crystalline-like structures often depicted in graphite staging models.

Upon discharge to the 2.15 V (point E), the chloroaluminate anions begin to electrochemically deintercalate, but the average ²⁷Al shift associated with intercalated anions remains nearly identical at 78.2 ppm. Interestingly, the lineshape narrows (FWHM of 72 ppm), reflecting modestly less disordered environments. This result is consistent with preferential deintercalation of chloroaluminate anions near the edges of the particles during this part of the discharge process. These edgesites are expected to be more disordered, on average. Further discharge to 1.60 V (point F) results in ²⁷Al shift at 70.6 ppm, and full discharge to 0.20 V (point G) results in a 27Al NMR signal of lower intensity centered at 46.8 ppm that is likely due to "trapped" chloroaluminate species in distorted environments within the graphite layers. This spectroscopic result is consistent with our prior electrochemical measurements,4 which establish additional capacity observed during the first charge, which may be associated partly or completely with trapped chloroaluminate anions. As discussed below, the ²⁷Al shifts of these trapped ions are consistent with chloroaluminate anions in more distorted geometries, which may be expected for trapped species. These NMR results also agree with in operando XRD results of Wang et al., 10 which show negligible changes in the graphite structure upon discharging from 2.45 V (point D) to 2.15 V (point E), but from 2.15 V to 1.60 V (point F) show significant contraction of the graphite d-spacing that would be expected to distort ions trapped locally within the bulk graphite cathode.

The solid-state 27 Al longitudinal T_1 NMR relaxation times of the intercalated chloroaluminate anions (Fig. 3c) yield information consistent with their molecular mobilities and the extents of local disorder. ²⁷Al longitudinal relaxation is dominated by the electric quadrupolar interaction, wherein local motions of the chloroaluminate anions cause the local EFG and hence quadrupolar interactions to fluctuate stochastically, a non-coherent process that forces the ²⁷Al spins to relax to thermal equilibrium. Hence, the 27 Al T_1 relaxation times are linked to molecular motions, where relaxation is most efficient (lower T_1) when the correlation time of motion is of the order of the inverse Larmor frequency $(1/\omega_0)$, which is on the order of nanoseconds. Mono-exponential ²⁷Al longitudinal relaxation behavior was observed for the intercalated $AlCl_4^-$ anions with T_1 values on the order of 10 ms. These relaxation times are 2 orders-of-magnitude greater compared to the 27 Al T_1 of AlCl₄ $^$ ions within the bulk electrolyte (200 µs), consistent with their reduced mobilities within the graphite layers. The 27 Al T_1 relaxation times of the intercalated AlCl₄⁻ anions decreased during charge (from 36.5 to 18.8 ms) and subsequently increases during discharge (from 9.3 to 23.0 ms). Interestingly, the 27 Al T_1 values exhibited a similar trend to the 27 Al linewidths, a correlation that indicates that ²⁷Al longitudinal NMR relaxation behavior is linked to the extent of local disorder. Indeed, for graphite electrodes charged to 1.90 V, 2.15 V, and 2.45 V, then discharged to 2.15 V and 1.60 V (i.e., points B through F), a smaller ²⁷Al linewidth correlates with shorter ²⁷Al T_1 relaxation times, suggesting that chloroaluminate anions in less disordered, more uniform environments exhibit greater local mobility. Note that fluctuating ²⁷Al-²⁷Al magnetic dipoledipole couplings, arising from intermolecular interactions among neighboring intercalated AlCl₄ anions, are another source of relaxation but are of secondary importance compared to intramolecular electric quadrupolar interactions.

As mentioned above, additional broad ²⁷Al NMR signals exist whose ²⁷Al shifts are consistent with octahedrally-coordinated aluminum moieties.56 The origin of these signals is unclear. At 2.45 V (point D), the 27 Al signal is centered at -27.4 ppm and accounts for 5% of the overall aluminum within the electrode. While it is possible that exposure to air could result in octahedral moieties such as AlO₆, these signals only appear at higher voltages (2.15 V and above), i.e., higher extents of chloroaluminate intercalation.

To detect possible Knight-shifted ²⁷Al signals in metallic environments, solid-state ²⁷Al MAS NMR measurements were acquired on a fully intercalated graphite electrode (2.45 V) at varying carrier frequencies (± 1600 ppm and ± 3200 ppm). Such signals have been observed in solid-state NMR studies of lithium-ion-intercalated^{26,57} and sodium-ion-intercalated^{32,33} graphitic compounds, which indicated the reversible formation of quasi-metallic clusters due to ion aggregation at high loadings. Here, Knight-shifted ²⁷Al signals were not detected over a broad frequency range, establishing that no quasi-metallic aluminum clusters were formed. Note that aluminum metal has a ²⁷Al NMR shift of approximately 1640 ppm, as shown in a solid-state ²⁷Al single-pulse MAS NMR spectrum of metallic aluminum powder (Fig. S4†). The absence of quasi-metallic aluminum is expected and consistent with the intercalation of molecular chloroaluminate anions into graphite, rather than atomic Al³⁺ cations.

Quantitative interpretations of experimental ²⁷Al NMR shifts using DFT calculations.

The intercalated chloroaluminates exhibit ²⁷Al signals that depend upon a combination of different NMR interactions: (i) chemical shift, (ii) nucleus-independent chemical shift, and (iii) electric quadrupolar couplings. We employ DFT methods to quantitatively disentangle the relative contributions of these NMR interactions to the experimental ²⁷Al NMR shifts and better understand the molecular-level environments of the intercalated chloroaluminate anions.

The total ²⁷Al isotropic NMR shift is the sum of each of these contributions:

$$\delta_{\rm iso}^{\rm total} = \delta_{\rm iso}^{\rm CS} + \delta_{\rm iso}^{\rm NICS} + \delta_{\rm iso}^{\rm 2Q} \tag{1}$$

where $\delta_{\rm iso}^{\rm total}$ is the total isotropic shift, $\delta_{\rm iso}^{\rm CS}$ is the isotropic chemical shift, $\delta_{\rm iso}^{\rm NICS}$ is the isotropic nucleus-independent chemical shift, and δ_{iso}^{2Q} is the second-order isotropic quadrupolar shift.

The chemical shift is an intramolecular diamagnetic shielding effect; electrons that surround each nucleus circulate in an applied magnetic field. The motion of these electrons induces a magnetic field that opposes the externally applied one, causing magnetic shielding of the nucleus. The nucleusindependent chemical shift is an intermolecular diamagnetic shielding effect, where magnetic shielding arises from ring currents due to the motions of delocalized electrons in conjugated systems, such as graphite. While both interactions involve magnetic shielding, only the chemical shift of a nucleus depends upon its local electronic bonding environment. The quadrupolar coupling is an electric interaction between the nuclear electric quadrupole moment of a nucleus with spin I > I1/2 and the local EFG at the nucleus.

The above solid-state NMR results establish that the intercalated chloroaluminate anions experience a wide variety of environments, many of which are far from those in ordered environments. This motivates the need to understand chloroaluminates in non-ideal, distorted geometries. Note that XRD only measures structures with long-range periodic ordering (i.e. able to coherently scatter X-rays) such as graphite layers with well-defined d-spacings that are associated with graphite staging, conditions which are not necessarily achieved locally, or at low extents of intercalation. Therefore, XRD does not capture dilute staging or local disorder, while coherent diffraction of the intercalated chloroaluminates themselves have not been reported. Furthermore, d-spacings derived from in operando XRD measurements vary^{2,6,10} because they employed models that require the assumption of a single, ideal stage number n, rather than a more realistic mixed-stage configuration.15

To capture the local disorder measured experimentally by solid-state NMR, we modeled chloroaluminates intercalated in between coronene or coronene-based sheets with decreasing interlayer spacings (from 10.5 Å to 6.5 Å, Fig. 4) to simulate how they deviate from the tetrahedral geometry due to interactions with the graphite layers.58 For each interlayer spacing, the AlCl₄⁻ molecular geometry is re-optimized to minimize the formation energy of the [AlCl₄⁻]-coronene bilayer structure. Note that structural or chemical defects present in graphite, such as edges, carbon vacancies, and oxygen impurities, are other sources of disorder that are not modeled here.

Calculated ²⁷Al chemical shift

To compute the ²⁷Al chemical shift, first the principal components $(\sigma_{xx}, \sigma_{yy}, \text{ and } \sigma_{zz})$ of the chemical shielding tensor $\boldsymbol{\sigma}$ within

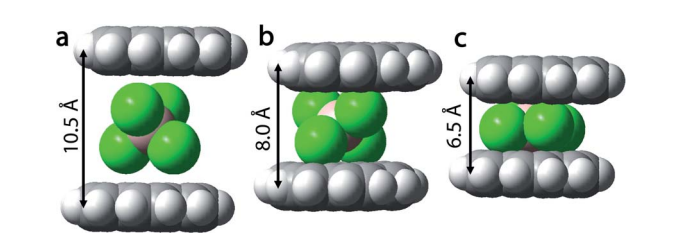


Fig. 4 Space-filling models of DFT-optimized [AlCl₄⁻]-coronene bilayer structures with varying interlayer spacings and degrees of geometric distortion. Van der Waals volumes are shown for the AlCl₄ anion.

its principal axis system are calculated for the optimized structure. The isotropic shielding constant

$$\sigma_{\rm iso} = \frac{\sigma_{\rm xx} + \sigma_{\rm yy} + \sigma_{\rm zz}}{3} \tag{2}$$

describes the magnetic shielding at the 27 Al nucleus in the AlCl $_4$ ⁻ anion. The DFT-calculated chemical shielding constant $\sigma_{\rm iso}$ can be converted to a DFT-calculated isotropic chemical shift $\delta_{\rm iso}^{\rm CS}$ via

$$\delta_{\rm iso}^{\rm CS} = \sigma_{\rm iso}^{\rm reference} - \sigma_{\rm iso} \tag{3}$$

where $\sigma_{\rm iso}^{\rm reference}$ is the DFT-calculated shielding of the ²⁷Al NMR reference standard (for [Al(H₂O)₆]³⁺, $\sigma_{\rm iso}^{\rm reference}$ = 611 ppm).⁵⁹ Using this reference standard yields $\delta_{\rm iso}^{\rm AlCl_4-}$ = 102 ppm for an AlCl₄⁻ anion, similar to the experimental ²⁷Al NMR shift of 103.2 ppm for AlCl₄⁻ in the bulk electrolyte.

The 27 Al chemical shift was modeled using coronene bilayer interlayer spacings from 10.5 Å to 6.5 Å (Table 1, Fig. 5a). At a large graphite d-spacing of 10.5 Å (Fig. 5a), the optimized molecular geometry is tetrahedral, yielding a high shielding constant ($\sigma_{\rm iso}=513.3$ ppm) that corresponds to a 27 Al isotropic chemical shift $\delta_{\rm iso}^{\rm CS}$ of 97.7 ppm. As the interlayer spacing is reduced, the AlCl $_4$ experiences increasing deviations from tetrahedral geometry. For example, enforcing an interlayer spacing of 6.5 Å results in near-planar geometry and a lower shielding constant ($\sigma_{\rm iso}=494.4$ ppm) that corresponds to a greater 27 Al isotropic chemical shift $\delta_{\rm iso}^{\rm CS}$ of 116.6 ppm. This higher chemical shift value is a result of decreased electron density around the 27 Al nucleus due to altered bond lengths and bond angles from those of the tetrahedral geometry of AlCl $_4$.

Calculated nucleus-independent chemical shift

To estimate the shift contribution due to ring-current effects from the graphite layers, NICS^{38,39} calculations were performed using a "ghost" atom to probe the local effective magnetic field between a coronene-based bilayer structure. Since aromatic ring-currents have an effect whose magnitude depends on the domain size of the graphene sheets,³⁹ a coronene bilayer model will underestimate the magnitude of the NICS value

experienced by intercalated AlCl₄ anions (Fig. S3a†). Therefore, a larger coronene-based graphene sheet (C150H30, lateral diameter of 22.2 Å) was used to better simulate the larger ab crystallite dimensions of natural graphite.4 NICS values $\delta_{\rm iso}^{\rm NICS}$ were computed for interlayer spacing varying from 10.5 Å to 6.5 Å (Table 1, Fig. 4b). Note that NICS values do not require a reference nucleus. As the interlayer spacing decreased, the magnitude of NICS increased due to increased molecular proximity of the ²⁷Al nucleus and the coronene-based sheets. For example, bilayers with interlayer spacings of 10.5 and 6.5 Å yielded NICS values of -13.1 and -17.5 ppm, respectively (Table 1). Note that ring currents contribute to magnetic shielding and serve to reduce the ²⁷Al isotropic shift, which are in qualitative agreement with the fact that the ²⁷Al NMR shifts of the intercalated AlCl₄⁻ anions resonate at lower frequency compared to that of the AlCl₄ in the bulk electrolyte (Fig. 1).

Additionally, the NICS values varied with lateral displacement of the atom for a constant d-spacing, since ring-currents induce shielding above/below the ring and deshielding in the periphery of the ring. For example, using a coronene bilayer model to illustrate this concept with an interlayer spacing of 9.2 Å, the NICS value is -4.8 ppm at the center, but more deshielded (-0.2 ppm) at the periphery (Fig. S3b†). The shift contribution from lateral displacement of anions is expected to be proportionally small, since edge sites are only a small fraction of all available graphite interlayer space. Therefore, we ignore this effect and assume the central position (x = 0) of the bilayer model for subsequent analyses.

Calculated ²⁷Al quadrupolar shift

Distortions of the molecular geometry of the intercalated $AlCl_4^-$ anion will influence the electric quadrupolar coupling interaction between the ^{27}Al nucleus and the local EFG, which will result in a quadrupolar shift that reduces the total ^{27}Al isotropic shift. 60,61 DFT calculations of the optimized molecular structure enable the EFG tensor to be computed at the ^{27}Al nucleus. 37 The Hamiltonian H_O describing this interaction is

$$H_{\mathbf{Q}} = \frac{eQ}{2I(2I-I)\hbar} \mathbf{I} \cdot \mathbf{V} \cdot \mathbf{I} \tag{4}$$

Table 1 DFT-computed NMR parameters for [AlCl₄⁻]-coronene-based bilayer systems with varying interlayer spacings

Interlayer spacing (Å)	shielding	Isotropic chemical shift $\left(\delta_{\mathrm{iso}}^{\mathrm{CS}}, \mathrm{ppm}\right)$	EFG tensor principal component $(V_{zz}, \text{ atomic units})$	Quadrupolar coupling constant (C_Q, MHz)	Quadrupolar asymmetry parameter (η)	quadrupolar shift	Nucleus independent chemical shift $(\delta_{ m iso}^{ m NICS}, { m ppm})$	Total Calculated Isotropic shift $(\delta_{ m iso}^{ m total}, { m ppm})$
6.5	494.4	116.6	-0.484	-16.8	0.24	-71.1	-17.5	28.0
7	502.9	108.1	-0.377	-13.1	0.15	-42.7	-16.9	48.6
7.5	507.7	103.4	-0.240	-8.4	0.10	-17.2	-16.3	69.9
8	510.4	100.7	-0.146	-5.1	0.05	-6.4	-15.7	78.6
8.5	511.8	99.2	-0.0750	-2.6	0.13	-1.7	-15.2	82.3
9	512.5	98.5	-0.0298	-1.0	0.28	-0.3	-14.6	83.6
9.2	512.6	98.4	-0.0188	-0.7	0.57	-0.1	-14.4	83.9
9.5	512.7	98.3	0.000	0.0	0.06	0.0	-14.1	84.2
10	513.0	98.0	0.000	0.0	0.00	0.0	-13.6	84.4
10.5	513.3	97.7	0.000	0.0	0.01	0.0	-13.1	84.6

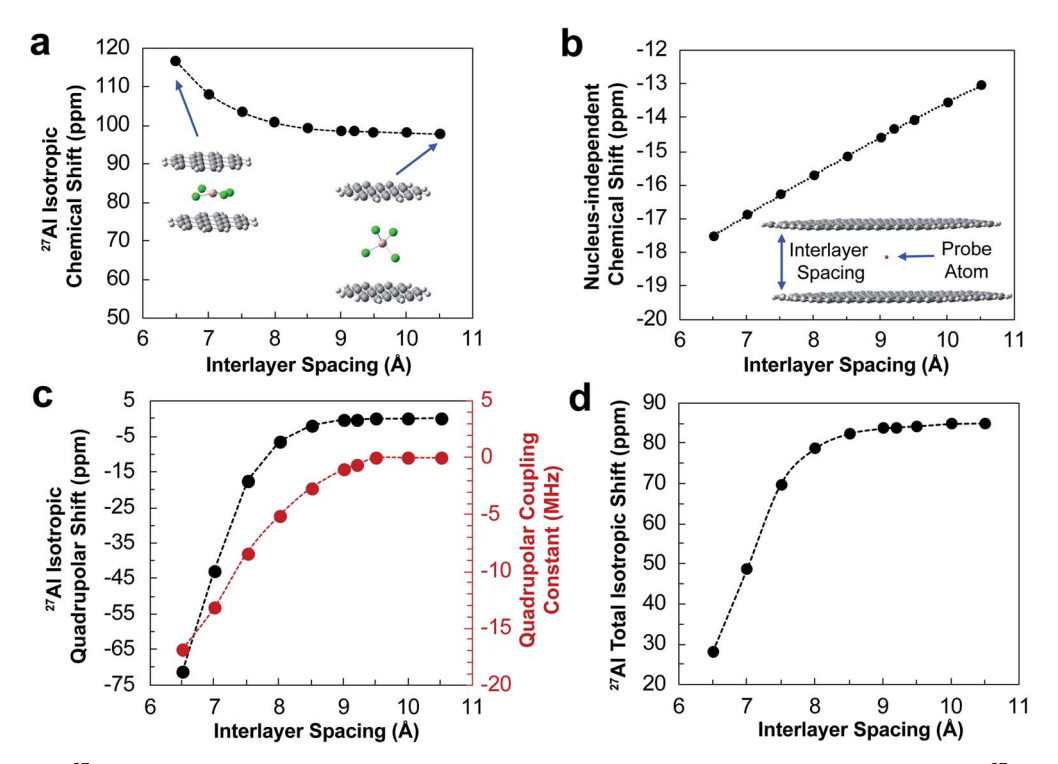


Fig. 5 DFT-calculated ²⁷Al parameters of [AlCl₄]-coronene-based bilayer systems with varying interlayer spacing. (a) ²⁷Al isotropic chemical shift ($\delta_{\rm iso}^{\rm iSS}$) (inset: optimized structures), (b) isotropic nucleus-independent chemical shift ($\delta_{\rm iso}^{\rm NICS}$), (c) ²⁷Al isotropic quadrupolar shift (black, $\delta_{\rm iso}^{\rm 2Q}$) and quadrupolar coupling constant (red, $C_{\rm Q}$), and (d) ²⁷Al total isotropic shift ($\delta_{\rm iso}^{\rm total}$). Dashed lines are shown to guide the eye.

where e is the elementary charge, Q is the nuclear electric quadrupole moment of the nucleus (for 27 Al, $Q=148.2\pm0.5$ mb), 62 \hbar is reduced Planck's constant, I is the nuclear spin quantum number, I is the nuclear spin operator, and V is the EFG tensor. The nuclear quadrupole coupling constant C_Q quantifies the magnitude of the quadrupolar interaction via

$$C_{\rm Q} = \frac{eQV_{\rm zz}}{h} \tag{5}$$

where h is Planck's constant, $V_{\rm zz}$ is the principal component (eigenvalue) within its principal axis system with the largest magnitude of the traceless EFG tensor (by convention, $|V_{\rm zz}| \ge |V_{\rm yy}| \ge |V_{\rm xx}|$).^{63,64} The EFG tensor is also characterized by the quadrupolar asymmetry parameter η defined as.

$$\eta = \frac{V_{xx} - V_{yy}}{V_{zz}} \tag{6}$$

The quadrupolar interaction can be expressed as a first-order and second-order perturbation to the Zeeman Hamiltonian. The first-order term splits the spectrum into 2*I*-1 satellite lines. This term does not affect the central transition and its effects are averaged by MAS. The second-order term is not completely removed by MAS and will alter the shift of the central transition. The isotropic quadrupolar shift ($\delta_{\rm iso}^{2Q}$) is determined from the quadrupolar parameters η and $C_{\rm Q}$ (Table 1) for a polycrystalline sample via

$$\delta_{\rm iso}^{\rm 2Q} \ [\rm ppm] = -\frac{3}{40} \left(\frac{C_{\rm Q}}{\omega_{\rm L}}\right)^2 \frac{I(I+1) - \frac{3}{4}}{I^2 (2I-I)^2} \left(1 + \frac{\eta^2}{3}\right) \times 10^6 \tag{7}$$

where $\omega_{\rm L}$ is the Larmor frequency of the 27 Al nuclei. 61,63,66

The second-order 27 Al quadrupolar shifts were computed using coronene bilayer interlayer spacings that varied from 10.5 Å to 6.5 Å (Table 1, Fig. 5c). When the graphite d-spacing is 10.5 Å, the tetrahedral geometry of the optimized $AlCl_4^-$ ion yields a C_Q of ca. 0 MHz (Fig. 5c) and therefore a negligible δ_{iso}^{2Q} . When the graphite interlayer spacing decreases, the increasing deviation from the tetrahedral geometry increases the EFG. For example, at 6.5 Å, DFT calculations yielded a higher V_{zz} value of -0.48 (Table 1). The large EFG indicates high deviation from the symmetric, tetrahedral geometry of the energy-optimized $AlCl_4^-$ structure, yielding a large C_Q of -16.8 MHz (Table 1). 11,58 Consequently, the large isotropic quadrupolar shift δ_{iso}^{2Q} of -71.1 ppm will shift the NMR signal to lower frequency.

Calculated total ²⁷Al isotropic shift

The calculated total isotropic shift $\delta_{\rm iso}^{\rm total}$ is the sum of the individual contributions modelled above (eqn (1)), whose values (Table 1, Fig. 5d) can be compared to the average experimental 27 Al NMR shifts (Fig. 3a). When the interlayer spacing is decreased from 10.5 Å to 6.5 Å, the calculated 27 Al shift decreases from 84.6 to 28.8 ppm, respectively (Table 1). The reported graphite d-spacings for chloroaluminate-intercalated graphite electrodes range from ca. 8.8 Å to 10.8 Å (obtained via DFT, 11,15,18 XRD^{6,10} and molecular dynamics (MD) simulations 14,58). For example, in operando XRD measurements by Wang et al. 10 indicate that chloroaluminate-intercalated graphite at full charge exhibits long-range ordering with d-spacing of 9.2 Å. If we also assume an average interlayer spacing

of ca. 9.2 Å, then the total calculated ^{27}Al isotropic shift $\delta_{\rm iso}^{\rm total}$ is 83.9 ppm, or 5.6 ppm greater than the average experimental ^{27}Al NMR shift of 78.3 ppm. This difference in absolute shift is discussed below. The trend in calculated ^{27}Al shifts at different interlayer spacings reveals insights into how the local environments of intercalated chloroaluminate change in distorted geometries.

Each total ²⁷Al isotropic shift $\delta_{\rm iso}^{\rm total}$ captures the local electronic and magnetic environments at the ²⁷Al nucleus when analyzed in terms of the underlying shifts $\delta_{\rm iso}^{\rm CS}$, $\delta_{\rm iso}^{\rm 2Q}$ and $\delta_{\rm iso}^{\rm NICS}$, enabling the dominant contributions to be disentangled among competing effects. For example, an ${\rm AlCl_4}^-$ anion intercalated within a coronene bilayer at an interlayer spacing of 6.5 Å has a highly-deshielded $\delta_{\rm iso}^{\rm CS}$ due to its near-planar geometry ($\delta_{\rm iso}^{\rm CS}=116.6~{\rm ppm}$), reflective of changes in intramolecular bond lengths and angles compared to tetrahedral geometry. Simultaneously, this distortion results in a large EFG and hence a large second-order quadrupolar shift ($\delta_{\rm iso}^{\rm 2Q}=-71.1~{\rm ppm}$). Meanwhile, the molecular proximity between the ²⁷Al nucleus and the coronene rings induces strong ring-current effects ($\delta_{\rm iso}^{\rm NICS}=-17.5~{\rm ppm}$). Collectively, these effects decrease the total ²⁷Al shift to lower values ($\delta_{\rm iso}^{\rm total}=28.0~{\rm ppm}$).

The discrepancies between the calculated and average experimental ²⁷Al NMR shifts are a result of the simplicity of the DFT model, which differ by approximately 5 to 6 ppm for the fully intercalated electrodes (2.45 V) assuming an interlayer spacing of 9 to 10 Å. First, the magnitude of NICS increases (more negative ppm values) when larger coronene-based sheets (e.g., Circumcoronene, Dicircumcoronene, C₁₅₀H₃₀ and $C_{216}H_{36}$) are used to model the graphite structure (Fig. 6). When the diameters of the coronene-based sheets increase, the DFTcalculated NICS values begin to asymptote. According to Kilymis et al.,41 the NICS value will approach a value of approximately -17 ppm for a C₂₉₄H₄₂ bilayer with an interlayer spacing of 9.2 Å. Thus, at an interlayer spacing of 9.2 A, using larger coronene-based sheets would thus result in a total ²⁷Al isotropic shift of ca. 81 ppm, comparing favorably to the average ²⁷Al shift of 78.3 ppm. Adding parallel graphene sheets above and below the bilayer to simulate graphite staging would also add an additional correction. Second, the model consists of an isolated AlCl₄ molecule and therefore neglects intermolecular interactions among adjacent intercalated anions. Intermolecular interactions may affect the local molecular geometries of AlCl₄ anions, perturbing their chemical and quadrupolar shifts. Note that homonuclear ²⁷Al-²⁷Al magnetic dipole-dipole couplings among intercalated AlCl₄ molecules will not affect the ²⁷Al isotropic shift, as the dipolar Hamiltonian is traceless, but may still contribute to line broadening at 10 kHz MAS. Similarly, bulk magnetic susceptibility (BMS) effects, 25,67-69 which arise from electron-nuclear dipolar coupling interactions and result in local magnetic field inhomogeneities, are not expected to affect appreciably the ²⁷Al shift. Anisotropic BMS effects due to the ellipsoidally-shaped (non-spherical) graphite particles could in principle alter the isotropic shift,68 though such effects are expected to be negligible at 10 kHz MAS. Notably, the residual electrolyte in contact with the graphite particle surfaces (27Al signal at 103 ppm, Fig. 2) resonates at the same frequency as the

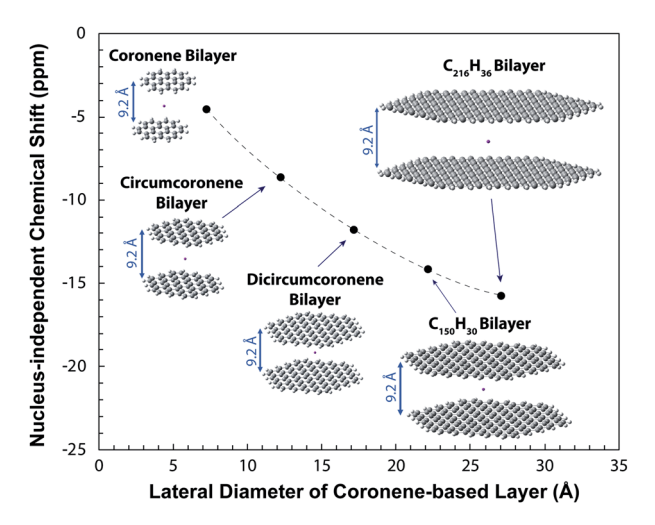


Fig. 6 Nucleus-independent chemical shift (NICS) values, associated with ring-current effects calculated for coronene-based bilayer models with different lateral dimensions. The interlayer spacing is fixed at 9.2 Å.

bulk electrolyte (Fig. 1), indicating that BMS effects do not contribute appreciably to the shift.

The range of DFT-calculated ²⁷Al isotropic NMR shifts (Table 1) is consistent with the broad ²⁷Al NMR linewidths observed experimentally. Each calculated $\delta_{\rm iso}^{\rm total}$ value represents a single AlCl₄ environment, whereas experimentally broad distributions of local 27Al environments are observed that reflect heterogeneity that may be understood, in part, by variations in local AlCl₄⁻ molecular geometries and local interlayer spacings. This distinction is manifested in the significant difference between the measured 27 Al transverse T_2 NMR relaxation times and the apparent time T_2^* associated with Fourier transform of the free induction decay (FID) under MAS alone, i.e., the linewidth. For example, the graphite electrode charged to 2.45 V (Fig. 2, point D) has a measured 27 Al T_2 of 660 μ s, while the value calculated from the linewidth⁷⁰ alone (90 ppm, or 54 kHz, Fig. 3b, point D) yields a much shorter T_2^* value of 5.9 µs. While dephasing of spin coherence can be the result of multiple effects, to a first approximation, the linewidth of a single intercalated AlCl₄ environment is estimated to be 2 orders-ofmagnitude narrower than the broad ²⁷Al signal observed.

Chloroaluminate anion intercalation mechanism

By analyzing the experimental solid-state NMR measurements in conjunction with the theoretical quantum chemical calculations, a physical picture emerges of the reversible electrochemical intercalation of $AlCl_4^-$ anions into graphite electrodes. When the cell is initially charged to 1.90 V (point B, Fig. 2), the ^{27}Al NMR shift at 56.7 ppm indicates that the average local geometry of an intercalated $AlCl_4^-$ anion is highly distorted, compared to tetrahedral configurations, presumably because the ions must overcome the van der Waals forces necessary to open the graphite interlayers. Indeed, at this potential, dilute (non-ordered) graphite staging occurs, 55,71 while non-diffusion-limited ion intercalation suggests shallow

penetration depths.4 The results indicate that before the graphite layers expand to form ordered stages, the intercalating ions adapt distorted molecular geometries, which may be a key component to understanding the high-rate capabilities demonstrated for these batteries. Increasing the cell voltage to 2.25 V (point C) and then 2.45 V (point D) results in greater extents of AlCl₄⁻ intercalation and average ²⁷Al NMR shifts of ca. 78 ppm. The ²⁷Al NMR shifts indicate that the larger interlayer spacings permit AlCl₄ anions with less distorted, neartetrahedral geometries, which in particular reduces the local EFG and hence quadrupolar shift. Discharge to 2.15 V results in ion deintercalation, yet the average ²⁷Al NMR shift remains ca. 78 ppm (point E), indicating similar average chloroaluminate environments. During discharge to 1.60 V (point F), further ion deintercalation occurs and the average ²⁷Al NMR shift decreases to 70.6 ppm, indicating that the average AlCl₄⁻ anion is slightly distorted. Further discharge to 0.20 V (point G, Fig. 2) deintercalates the majority of AlCl₄ ions, though some trapped ions remain⁴ due to the contraction of the graphite *d*-spacing to ~3.3 Å upon full discharge, as shown by in operando XRD.¹⁰ These trapped AlCl₄⁻ anions exhibit average ²⁷Al NMR shifts of 48.8 pm, consistent with highly distorted molecular geometries and large EFGs at the ²⁷Al nuclei that decrease the ²⁷Al isotropic shift.

Conclusions

Solid-state ²⁷Al MAS NMR spectroscopy was used to probe the molecular-level environments of $AlCl_4^-$ chloroaluminate anions intercalated within graphite battery electrodes at different states-of-charge. The broad ²⁷Al NMR signals of the intercalated chloroaluminate anions reveal experimentally the breadth of local disorder in graphite intercalation electrodes, which is not captured in diffraction analyses or ideal staging models. The ²⁷Al NMR shifts and linewidths vary with different extents of ion intercalation. DFT calculations were performed to interpret the ²⁷Al shifts in terms of the local electronic and magnetic environments of intercalant anions. The intercalant-electrode system was modeled as an [AlCl₄-]-coronene-based bilayer structure, where the interlayer spacing was varied to simulate environments that distort the molecular geometry of the AlCl₄ anion. The DFT calculations enable the total ²⁷Al isotropic NMR shifts to be understood quantitatively in terms of chemical shift, ring-current effects (nucleus-independent chemical shift), and electric quadrupolar interactions (quadrupolar shift). The results establish that the high extents of local disorder observed in the solid-state ²⁷Al NMR spectra are in large part due to distributions of AlCl₄⁻ anions in different molecular configurations. In addition, the results suggest that the chloroaluminate anions can intercalate even before the graphite layers expand to form ordered stages by adapting distorted molecular geometries, which may be a key component to understanding the high-rate capabilities demonstrated in aluminum-graphite batteries. The solid-state ²⁷Al NMR results establish unambiguously the presence of "trapped" chloroaluminate anions after discharge (deintercalation), which reside in the most distorted environments and reduce the

capacity of the electrode in subsequent cycles. Overall, the combined solid-state NMR and DFT results reveal a more nuanced molecular-level understanding of the local environments of intercalated chloroaluminate anions, establishing large extents of local disorder far from the ideal crystalline-like structures often depicted in graphite staging models.

Conflicts of interest

The authors declare no conflicts of interest.

Acknowledgements

The authors gratefully acknowledge support from the U.S. National Science Foundation (NSF) under grant no. CBET-170692. The authors thank Prof. Alexander C. Forse (University of Cambridge, UK) for fruitful discussions regarding DFT modeling and NMR parameter calculations. NMR measurements were performed at the City University of New York (CUNY) Advanced Science Research Center. DFT calculations were performed at the CUNY High Performance Computing Center at the College of Staten Island, which is supported in part by NSF awards CNS-0958379, CNS-0855217, and ACI-1126113.

Notes and references

- 1 D. Wang, C. Wei, M. Lin, C. Pan, H. Chou, H. Chen, M. Gong, Y. Wu, C. Yuan, M. Angell, Y. Hsieh, Y. Chen, C. Wen, C. Chen, B. Hwang, C. Chen and H. Dai, *Nat. Commun.*, 2017, 8, 1–7.
- 2 M.-C. C. Lin, M. Gong, B. Lu, Y. Wu, D.-Y. Y. Wang, M. Guan, M. Angell, C. Chen, J. Yang, B.-J. J. Hwang and H. Dai, *Nature*, 2015, 520, 324–328.
- 3 H. Sun, W. Wang, Z. Yu, Y. Yuan, S. Wang and S. Jiao, *Chem. Commun.*, 2015, **51**, 11892–11895.
- 4 J. H. Xu, D. E. Turney, A. L. Jadhav and R. J. Messinger, ACS Appl. Energy Mater., 2019, 2, 7799–7810.
- 5 H. Chen, H. Xu, S. Wang, T. Huang, J. Xi, S. Cai, F. Guo, Z. Xu, W. Gao and C. Gao, *Sci. Adv.*, 2017, 3, eaao7233.
- 6 C.-J. Pan, C. Yuan, G. Zhu, Q. Zhang, C.-J. Huang, M.-C. Lin, M. Angell, B.-J. Hwang, P. Kaghazchi and H. Dai, *Proc. Natl. Acad. Sci. U. S. A.*, 2018, 115, 5670–5675.
- 7 L. Zhang, L. Chen, H. Luo, X. Zhou and Z. Liu, *Adv. Energy Mater.*, 2017, **2**, 1700034.
- 8 K. V. Kravchyk, S. Wang, L. Piveteau and M. V. Kovalenko, *Chem. Mater.*, 2017, 29, 4484–4492.
- 9 Y. Wu, M. Gong, M.-C. C. Lin, C. Yuan, M. Angell, L. Huang, D.-Y. Y. Wang, X. Zhang, J. Yang, B.-J. J. Hwang and H. Dai, *Adv. Mater.*, 2016, 28, 9218–9222.
- 10 D.-Y. Y. Wang, S.-K. K. Huang, H.-J. J. Liao, Y.-M. M. Chen, S.-W. W. Wang, Y.-T. T. Kao, J.-Y. Y. An, Y.-C. C. Lee, C.-H. H. Chuang, Y.-C. C. Huang, Y.-R. R. Lu, H.-J. J. Lin, H.-L. L. Chou, C.-W. W. Chen, Y.-H. H. Lai and C.-L. L. Dong, *Carbon*, 2019, 146, 528–534.
- 11 Y. Gao, C. Zhu, Z. Chen and G. Lu, *J. Phys. Chem. C*, 2017, **121**, 7131–7138.

- 12 M. S. Wu, B. Xu, L. Q. Chen and C. Y. Ouyang, *Electrochim. Acta*, 2016, **195**, 158–165.
- 13 P. Bhauriyal, A. Mahata and B. Pathak, *J. Phys. Chem. C*, 2017, **121**, 9748–9756.
- 14 M. L. Agiorgousis, Y.-Y. Sun and S. Zhang, *ACS Energy Lett.*, 2017, 689–693.
- 15 Q. Wang, D. Zheng, L. He and X. Ren, *Phys. Rev. Appl.*, 2019, **12**. 1.
- 16 M. S. Wu, B. Xu and C. Y. Ouyang, *Electrochim. Acta*, 2017, **223**, 137–139.
- 17 S. C. Jung, Y. J. Kang and Y. K. Han, *Electrochim. Acta*, 2017, **223**, 135–136.
- 18 J. Li, Q. Liu, A. Flores, J. Lemmon and T. Bligaard, *Phys. Chem. Chem. Phys.*, 2020, 22, 5969–5975.
- 19 T. Cosgrove, B. W. Copping and R. A. Jarvis, *J. Colloid Interface Sci.*, 1983, **96**, 214–221.
- 20 R. K. Harris, T. V Thompson, P. R. Norman and C. Pottage, *Carbon*, 1999, 37, 1425–1430.
- 21 L. Trognko, H. Wang, N. M. Trease, J. M. Griffin, P.-L. Taberna, C. P. Grey, P. Simon and A. C. Forse, *J. Am. Chem. Soc.*, 2013, 135, 18968–18980.
- 22 M. Oschatz, L. Borchardt, F. Hippauf, W. Nickel, S. Kaskel and E. Brunner, *Annu. Rep. NMR Spectrosc.*, 2016, **87**, 237–318.
- 23 H. Wang, T. K. J. Köster, N. M. Trease, J. Segalini, P.-L. Taberna, P. Simon, Y. Gogotsi and C. P. Grey, *J. Am. Chem. Soc.*, 2011, 19270–19273.
- 24 M. Deschamps, E. Gilbert, P. Azais, E. Raymundo-Piñero, M. R. Ammar, P. Simon, D. Massiot and F. Béguin, *Nat. Mater.*, 2013, 12, 351–358.
- 25 O. Pecher, J. Carretero-gonza, K. J. Gri and C. P. Grey, *Chem. Mater.*, 2017, 29(1), 213–242.
- 26 K. Guérin, M. Ménétrier, A. Février-Bouvier, S. Flandrois, B. Simon and P. Biensan, *Solid State Ionics*, 2000, 127, 187–198.
- 27 N. Imanishi, K. Kumai, H. Kokugan, Y. Takeda and O. Yamamoto, *Solid State Ionics*, 1998, **107**, 135–144.
- 28 M. Letellier, F. Chevallier, F. Béguin, E. Frackowiak and J. N. Rouzaud, *J. Phys. Chem. Solids*, 2004, **65**, 245–251.
- 29 A. I. Freytag, A. D. Pauric, S. A. Krachkovskiy and G. R. Goward, *J. Am. Chem. Soc.*, 2019, **141**, 13758–13761.
- 30 C. P. Grey and Y. J. Lee, Solid State Sci, 2003, 5, 883-894.
- 31 R. J. Messinger, M. Ménétrier, E. Salager, A. Boulineau, M. Duttine, D. Carlier, J. M. Ateba Mba, L. Croguennec, C. Masquelier, D. Massiot and M. Deschamps, *Chem. Mater.*, 2015, 27, 5212–5221.
- 32 K. Gotoh, T. Ishikawa, S. Shimadzu, N. Yabuuchi, S. Komaba, K. Takeda, A. Goto, K. Deguchi, S. Ohki, K. Hashi, T. Shimizu and H. Ishida, *J. Power Sources*, 2013, 225, 137–140.
- 33 J. M. Stratford, P. K. Allan, O. Pecher, P. A. Chater and C. P. Grey, *Chem. Commun.*, 2016, 52, 12430–12433.
- 34 P. M. Bayley, N. M. Trease and C. P. Grey, *J. Am. Chem. Soc.*, 2016, **138**, 1955–1961.
- 35 G. R. Miller, H. A. Resing, M. J. Moran, L. Banks, F. L. Vogel, A. Pron and D. Billaud, *Synth. Met.*, 1983, **8**, 77–82.

- 36 K. V. Kravchyk, P. Bhauriyal, L. Piveteau, C. P. Guntlin, B. Pathak and M. V. Kovalenko, *Nat. Commun.*, 2018, **9**, 4469.
- 37 R. W. Schurko, R. E. Wasylishen and A. D. Phillips, *J. Magn. Reson.*, 1998, **133**, 388–394.
- 38 Y. Z. Xing, Z. X. Luo, A. Kleinhammes and Y. Wu, *Carbon*, 2014, 77, 1132–1139.
- 39 A. C. Forse, J. M. Griffin, V. Presser, Y. Gogotsi and C. P. Grey, J. Phys. Chem. C, 2014, 118, 7508–7514.
- 40 D. Moran, F. Stahl, H. F. Bettinger, H. F. Schaefer and P. v. R. Schleyer, *J. Am. Chem. Soc.*, 2003, **125**, 6746–6752.
- 41 D. Kilymis, A. P. Bartók, C. J. Pickard, A. C. Forse and C. Merlet, *Phys. Chem. Chem. Phys.*, 2020, **22**, 13746–13755.
- 42 M. H. Ghatee and F. Moosavi, J. Phys. Chem. C, 2011, 115, 5626–5636.
- 43 F. A. L. de Souza, A. R. Ambrozio, E. S. Souza, D. F. Cipriano, W. L. Scopel and J. C. C. Freitas, *J. Phys. Chem. C*, 2016, 120, 27707–27716.
- 44 S. Miyoshi, T. Akbay, T. Kurihara, T. Fukuda, A. T. Staykov, S. Ida and T. Ishihara, *J. Phys. Chem. C*, 2016, **120**, 22887– 22894.
- 45 H. J. Liao, Y. M. Chen, Y. T. Kao, J. Y. An, Y. H. Lai and D. Y. Wang, *J. Phys. Chem. C*, 2017, **121**(44), 24463–24469.
- 46 K. Tasaki, J. Phys. Chem. C, 2014, 118, 1443-1450.
- 47 C. J. Yu, U. S. Ri, G. C. Ri and J. S. Kim, *Phys. Chem. Chem. Phys.*, 2018, **20**, 14124–14132.
- 48 D. Fenzke, D. Freude, T. Fröhlich and J. Haase, *Chem. Phys. Lett.*, 1984, **111**, 171–175.
- 49 D. Massiot, F. Fayon, M. Capron, I. King, S. Le Calvé, B. Alonso, J. O. Durand, B. Bujoli, Z. Gan and G. Hoatson, *Magn. Reson. Chem.*, 2002, **40**, 70–76.
- 50 M. J. Frisch, G. W. Trucks, H. B. Schlegel, G. E. Scuseria, M. A. Robb, J. R. Cheeseman, G. Scalmani, V. Barone,
 - G. A. Petersson, H. Nakatsuji, X. Li, M. Caricato,
 - A. Marenich, J. Bloino, B. G. Janesko, R. Gomperts, B. Mennucci, H. P. Hratchian, J. V. Ortiz, A. F. Izmaylov,
 - J. L. Sonnenberg, D. Williams-Young, F. Ding, F. Lipparini,
 - F. Egidi, J. Goings, B. Peng, A. Petrone, T. Henderson,
 - D. Ranasinghe, V. G. Zakrzewski, J. Gao, N. Rega,
 - G. Zheng, W. Liang, M. Hada, M. Ehara, K. Toyota,
 - R. Fukuda, J. Hasegawa, M. Ishida, T. Nakajima, Y. Honda, O. Kitao, H. Nakai, T. Vreven, K. Throssell,
 - J. A. Montgomery Jr, J. E. Peralta, F. Ogliaro, M. Bearpark,
 - J. J. Heyd, E. Brothers, K. N. Kudin, V. N. Staroverov,
 - T. Keith, R. Kobayashi, J. Normand, K. Raghavachari,
 - A. Rendell, J. C. Burant, S. S. Iyengar, J. Tomasi, M. Cossi,
 - J. M. Millam, M. Klene, C. Adamo, R. Cammi,
 - J. W. Ochterski, R. L. Martin, K. Morokuma, O. Farkas,
 - J. B. Foresman, and D. J. Fox, *Gaussian 09, Revision E.01*, Gaussian, Inc., Wallingford CT, 2016.
- 51 S. Grimme, J. Antony, S. Ehrlich and H. Krieg, *J. Chem. Phys.*, 2010, **132**, 154104.
- 52 M. D. Hanwell, D. E. Curtis, D. C. Lonie, T. Vandermeersch, Z. Eva and G. R. Hutchison, *J. Cheminf.*, 2012, 4–17.
- 53 S. Grimme, W. Hujo and B. Kirchner, *Phys. Chem. Chem. Phys.*, 2012, **14**, 4875–4883.
- 54 C. Ferrara, V. Dall'Asta, V. Berbenni, E. Quartarone and P. Mustarelli, *J. Phys. Chem. C*, 2017, **121**, 26607–26614.

- 55 R. B. Smith, E. Khoo and M. Z. Bazant, *J. Phys. Chem. C*, 2017, **121**, 12505–12523.
- 56 M. Haouas, F. Taulelle and C. Martineau, *Prog. Nucl. Magn. Reson. Spectrosc.*, 2016, **94–95**, 11–36.
- 57 J. Conard and H. Estrade, Mater. Sci. Eng., 1977, 31, 173-176.
- 58 P. Bhauriyal, A. Mahata and B. Pathak, *Phys. Chem. Chem. Phys.*, 2017, **19**, 7980–7989.
- 59 V. P. Tarasov and G. A. Kirakosyan, *Russ. J. Inorg. Chem.*, 2008, 53, 2048–2081.
- 60 P. P. Man, Quadrupolar Interactions, in *eMagRes*, ed. R. K. Harris and R. L. Wasylishen, 2011, DOI: 10.1002/9780470034590.emrstm0429.pub2.
- 61 A. Samoson, Chem. Phys. Lett., 1985, 119, 29-32.
- 62 A. Aerts and A. Brown, J. Chem. Phys., 2019, 150, 224302.
- 63 L. J. Criscenti, S. L. Brantley, K. T. Mueller, N. Tsomaia and J. D. Kubicki, *Geochim. Cosmochim. Acta*, 2005, 69, 2205– 2220.

- 64 T. Bräuniger, P. Kempgens, R. K. Harris, A. P. Howes, K. Liddell and D. P. Thompson, *Solid State Nucl. Magn. Reson.*, 2003, 23, 62–76.
- 65 K. Narita, J. Umeda and K. Hazime, *J. Chem. Phys.*, 1966, 44, 2719.
- 66 K. T. Mueller, J. H. Baltisberger, E. W. Wooten and A. Pines, J. Phys. Chem., 1992, 96, 7001–7004.
- 67 J. L. Bonardet and J. P. Fraissard, *J. Magn. Reson.*, 1976, 22, 543–548.
- 68 L. Zhou, M. Leskes, A. J. Ilott, N. M. Trease and C. P. Grey, *J. Magn. Reson.*, 2013, **234**, 44–57.
- 69 A. Kubo, T. P. Spaniol and T. Terao, *J. Magn. Reson.*, 1998, **133**, 330–340.
- 70 J. Furrer, K. Elbayed, M. Bourdonneau, J. Raya, D. Limal, A. Bianco and M. Piotto, *Magn. Reson. Chem.*, 2002, **40**, 123–132.
- 71 A. S. Childress, P. Parajuli, J. Zhu, R. Podila and A. M. Rao, *Nano Energy*, 2017, **39**, 69–76.

Supporting Information

Molecular-Level Environments of Intercalated Chloroaluminate Anions in Rechargeable Aluminum-Graphite Batteries Revealed by Solid-State NMR Spectroscopy

Jeffrey H. Xu, Ankur L. Jadhav, Damon E. Turney, and Robert J. Messinger*
Department of Chemical Engineering, The City College of New York, CUNY, New York, New York 10031, United States
*E-mail: rmessinger@ccny.cuny.edu

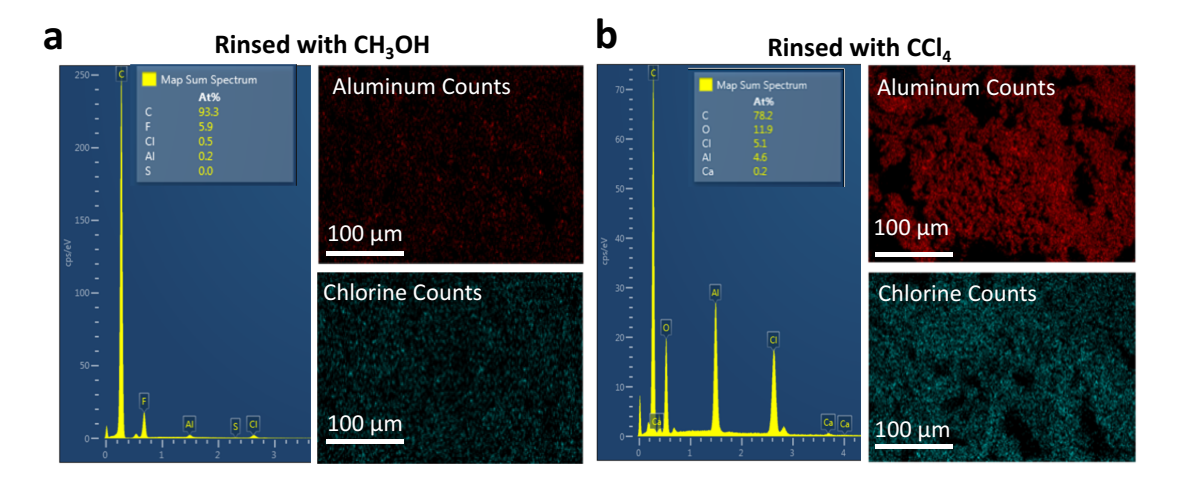


Figure S1. Scanning electron microscopy (SEM) images with energy dispersive X-ray spectroscopy (EDS) elemental mapping for graphite electrodes rinsed with (a) anhydrous methanol (CH₃OH) and (b) carbon tetrachloride (CCl₄), which were harvested from Al-graphite cells galvanostatically charged to 2.45 V at 60 mA/g. The results show that anhydrous methanol was more effective in washing away the excess AlCl₃:[EMImCl] (molar ratio 1.5:1) ionic liquid electrolyte from the surfaces of the harvested electrodes. Data was collected using a Helios NanoLab 660 SEM with an Oxford EDX detector.

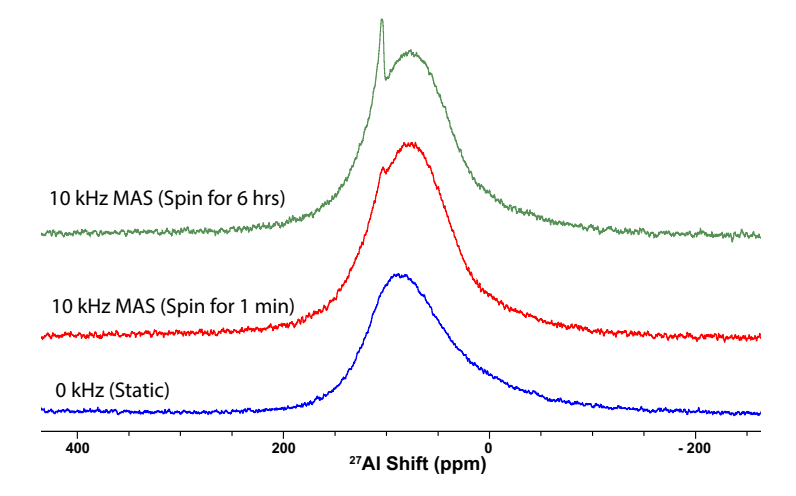


Figure S2. Solid-state 27 Al single-pulse MAS NMR spectra acquired on a fully intercalated graphite electrode, illustrating the effects of MAS on residual electrolyte. The electrode was harvested from an Al-graphite cell galvanostatically charged to 2.45 V at 60 mA/g and subsequently rinsed with anhydrous methanol. A static spectrum was initially acquired (blue), as well as one after 1 minute of MAS at 10 kHz (red). Electrolyte trapped within the electrode pores is gradually expelled due to centrifugal forces from sample rotation. The 27 Al signal at approximately 103 ppm, associated with AlCl₄ anions in the residual electrolyte, increased in intensity with increasing MAS time and then equilibrated. All solid-state 27 Al MAS NMR measurements reported in Figure 2 (main text) were acquired after spinning for 6 hours (green), when equilibration was achieved.

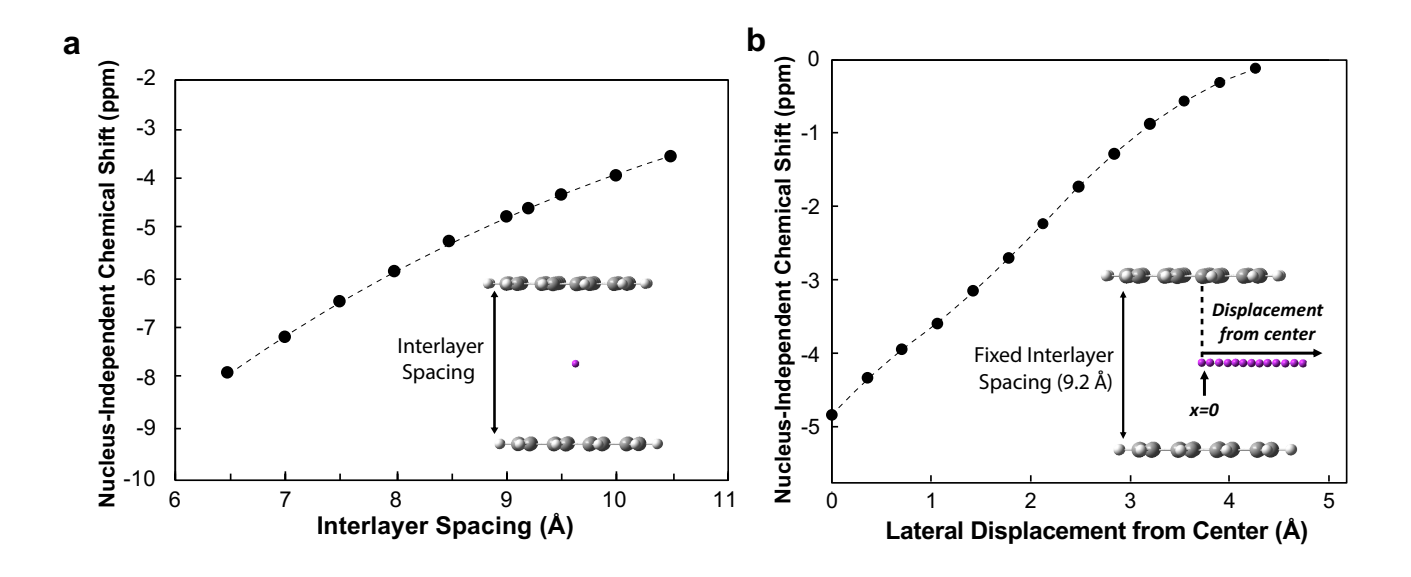


Figure S3. Nucleus-independent chemical shift (NICS) for a coronene bilayer (diameter = 7.3 Å) as a function of (a) interlayer spacing and (b) lateral displacement of the probe ("ghost") atom from the central position with fixed interlayer spacing of 9.2 Å. *Inset*: DFT-optimized structure of the coronene bilayer and illustration of the lateral displacement of the probe atom (purple). Dashed lines are shown to guide the eye.

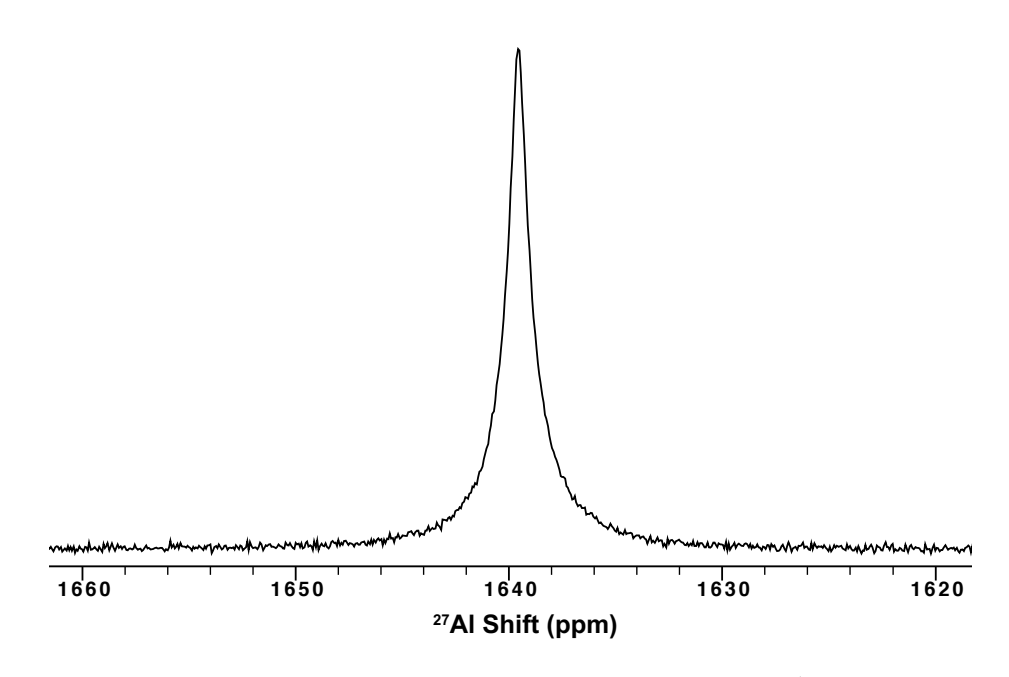


Figure S4. Solid-state 27 Al single-pulse MAS NMR spectrum of metallic aluminum powder (2 μ m diameter particles), acquired at 20 kHz MAS and 14.1 T, reveals a Knight-shifted signal at 1639 ppm associated with aluminum metal. The 27 Al shift was referenced to 1M aqueous Al(NO3)₃. To enable sample rotation in the magnetic field, the aluminum powder was diluted with KBr powder using a mass ratio of 1:9.

Table S1. DFT-calculations of the principle components of the traceless electric field gradient (EFG) tensor at the aluminum nucleus for the [AlCl₄-]-coronene bilayer system with varying interlayer spacings.

	Principle Components of Electric Field Gradient (EFG) Tensor (V)					
Interlayer spacing of [AlCl ₄]-coronene bilayer (Å)	V _{xx} (atomic units)	V _{yy} (atomic units)	V _{zz} (atomic units)			
6.5	0.1827	0.3012	-0.4839			
7	0.1596	0.2177	-0.3773			
7.5	0.1075	0.1327	-0.2402			
8	0.0698	0.0764	-0.1462			
8.5	0.0325	0.0425	-0.0750			
9	0.0107	0.0191	-0.0298			
9.2	0.0041	0.0147	-0.0188			
9.5	0.000088	0.0001	-0.00019			
10	0.000008	0.00008	-0.000015			
10.5	0.000176	0.000181	-0.000357			

References

1 A. C. Forse, J. M. Griffin, V. Presser, Y. Gogotsi and C. P. Grey, *J. Phys. Chem. C*, **2014**, *118*, 7508–7514.